IEEE Journal of Microwaves

Received 15 February 2024; revised 27 March 2024; accepted 10 June 2024. Date of publication 3 July 2024; date of current version 12 July 2024.

Digital Object Identifier 10.1109/JMW.2024.3414130

Monolithically-Integrated 3D Printed Bandpass Filters Using Highly-Miniaturized Dome-Shaped Resonators

KUNCHEN ZHAO[1] (Student Member, IEEE), CHRISTIAN ELMIGER[2], AND DIMITRA PSYCHOGIOU[3,4] (Senior Member, IEEE)

(Regular Paper)

[1]Department of Electrical, Computer, and Energy Engineering, University of Colorado Boulder, Boulder, CO 80309 USA
[2]Stryker, T45 HX08 Cork, Ireland
[3]Department of Electrical and Electronic Engineering, University College Cork, T12 K8AF Cork, Ireland
[4]Tyndall National Institute, T12 R5CP Cork, Ireland

CORRESPONDING AUTHOR: Dimitra Psychogiou (e-mail: DPsychogiou@ucc.ie).

This work was supported by Science Foundation Ireland under Grant 20/RP/8334 and Grant SFI-13/RC/2077.

ABSTRACT A new class of highly-miniaturized "dome"-shaped 3D bandpass filters (BPFs) are presented. Size reduction is achieved by using: i) capacitively-loaded hemispherical resonators that are significantly smaller than a conventional spherical resonator, ii) stereolithography apparatus (SLA)-based 3D printing facilitating monolithic integration, and by iii) vertically-stacked resonators. A comprehensive design methodology is provided and applied to the realization of high order BPFs. An RF excitation scheme allowing for wideband out-of-band suppression is also proposed. For proof-of-concept validation purposes, a second- and a third-order BPF prototypes operating at 5.8 GHz, and a compact vertically-stacked second-order BPF were designed, manufactured, and tested. The measurement results exhibit the following characteristics: second-order BPF: center frequency f_c = 5.8 GHz, fractional bandwidth (FBW) = 5.5%, effective quality factor (Q_{eff}) = 890, 20 dB upper stopband suppression up to 10.14 GHz (1.7.3f_c); third-order BPF: f_c = 5.8 GHz, FBW = 6.5%, Q_{eff} = 1,230, and 20 dB upper stopband suppression up to 10.1 GHz (1.74f_c); vertically-stacked second-order BPF: f_c = 5.9 GHz, FBW = 10.0%, Q_{eff} = 720, and 20 dB upper stopband suppression up to 8.9 GHz (1.5f_c)

INDEX TERMS Additive manufacturing, high-Q resonator, miniaturized filter, spherical resonator, 3D filter.

I. INTRODUCTION

The unprecedented growth of modern communication systems such as 5G has brought forth an increasing demand for multi-functional, high-performing, and compact RF transceivers. As the key enabling component for RF signal filtering in base-stations and radar systems, 3D bandpass filters (BPFs) need to support these requirements alongside having high quality factor (Q), high-power handling, small form factor, and low weight [1]. However, conventional cavity or waveguide resonator-based BPFs occupy a significant part of the available volume in an RF transceiver. This is due to the dimensions of their resonators being comparable to the wavelength, creating manufacturing, size, and weight challenges for RF applications at the lower end of the frequency spectrum.

To address these challenges, miniaturization and weight reduction techniques are increasingly explored for 3D BPFs. For example, the use of half-mode substrate integrated waveguides (SIWs) has been proposed in [2] to reduce the overall volume of SIW filter by 75%. However, such filters suffer from high insertion loss (effective quality factor Q_{eff}<100) due to being built on lossy dielectrics. Miniaturization techniques for dielectric [3], [4] and rectangular waveguide-based filters [5], [6] have also been proposed. In terms of spherical BPFs, despite being made by high-Q (>2000) resonators, they are large and hard to miniaturize. A limited number

of approaches have been presented for their miniaturization including using dual-mode [7], [8], [9], [10], [11], triple-mode [12], [13], and quint-mode [14] resonators where multiple resonant modes are combined within a single cavity to reduce the overall filter volume. However, the size of the resulting filters is fairly large. A preliminary post-loaded irregular-shape spherical resonator design was proposed in [15] for size miniaturization. However, it hasn't been used for the realization of BPFs. In yet another approach, a spherical BPF miniaturization was attempted using hemispherical resonators [16], [17], [18] leading to smaller volume when compared to conventional spherical-resonator-based BPFs.

Another challenge in the realization of 3D BPFs lies in their assembly and manufacturing. Specifically, spherical resonator-based BPFs can't be easily manufactured using all-metal CNC machining processes due to the irregularity of their shape [12], [13], [14], [15]. Thus, they are implemented as split blocks and are assembled with screws ending up being bulky and heavy. Furthermore, they require post fabrication tuning needing additional screws to be incorporated which further increases their weight and size alongside the required testing and assembly cycles.

Emerging additive manufacturing (AM) technologies or 3D printing are increasingly being explored as a manufacturing alternative to traditional CNC machining [19]. Plastic-based AM processes such as fused-deposition modeling (FDM) or stereolithography apparatus (SLA) have been widely employed for the fabrication of waveguide-based RF passive devices [20], [21], [22]. However, the majority of them has focused on split-block assemblies due to the need for internal metallization, which results in high radiation loss as well as increased size and weight due to the need for post-assembly and post-fabrication tuning. Furthermore, FDM processes lead to fairly rough surface profiles and aren't suitable for the realization of high-frequency RF components.

To further facilitate miniaturization of 3D RF BPFs, monolithic metal or plastic-based AM integration concepts are increasingly explored. Metal-based AM processes such as direct laser metal sintering (DLMS) [23] and selective laser melting (SLM) [24] are the most commonly used ones for monolithic integration of spherical resonator-based BPFs [9], [17], [25], [26], [27]. Although a decent performance has been achieved, such processes have high operational costs and lead to high surface roughness (common $R_a > 15\ \mu$m in [28]). SLA-based monolithic AM processes are increasingly being used for the realization of 3D RF components and due to their significantly lower surface roughness which makes them more suitable for high frequency implementations; however, they are mostly used for the realization of open-ended waveguide-based RF components [29]. Monolithic integration of fully-enclosed structures such as in coaxial cavity [30] or spherical/hemispherical filters [7], [8], [9], [10], [11], [17], [18] have recently been demonstrated using SLA, however they require non-radiating perforations to be added to facilitate the metal plating process.

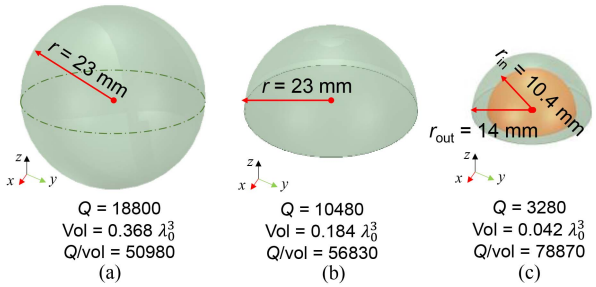

FIGURE 1. (a) Spherical resonator with fundamental resonance at 5.8 GHz. (b) Hemispherical resonator with fundamental resonance at 5.8 GHz. (c) The proposed "dome-shaped" resonator with fundamental resonance at 5.8 GHz, which is 84% smaller than the conventional spherical resonator and has a 54% higher *Q*/Vol. *Q* was obtained with eigenmode simulations using bulk Cu without roughness.

To address the aforementioned limitations, this paper presents for the first time a new class of monolithically-integrated 3D BPFs using "dome-shaped" resonators with high performance and the potential for high levels of miniaturization in the RF front-end. Filter miniaturization is achieved using: i) capacitively-loaded hemi-spherical resonators that are 85% smaller than a conventional spherical resonator, ii) monolithic SLA integration that facilitates monoblock manufacturing and doesn't require multiple parts or tuning and assembly screws, and iii) vertical and L-shaped integration which also contribute to enhanced out-of-band rejection of the filters' transfer-function. Two novel BPF architectures exhibiting a second and a third order transfer function and a spur suppression mechanism are demonstrated in this work for proof-of-concept demonstration purposes. Compared to conventional spherical filters, the proposed BPF concepts exhibit significantly smaller volume, improved spurious performance, and higher *Q*/Vol ratio. Moreover, an ultra-compact vertically-integrated BPF scheme is proposed for the first time exhibiting two controllable out-of-band transmission zeros (TZs). The proposed miniaturized filter concept is validated by two unique second-order and a third-order prototypes operating at C band. The manuscript is organized as follows. In Section II, the theoretical foundations of the proposed filter concept are presented. Section III outlines the experimental validation of the concept and Section IV reports on the major contributions of this work.

II. THEORETICAL FOUNDATIONS

In what follows, the theoretical foundations of the proposed dome resonator concept are set out using eigen-mode simulations. The concept is then validated through the design of a second, a third-order, and a compact second-order vertically-stacked BPF.

A. "DOME"-SHAPED HIGH-Q RESONATOR CONCEPT

The geometrical details of the proposed capacitively-loaded hemispherical dome-shaped resonator concept are illustrated in Fig. 1 for a center frequency of 5.8 GHz. The

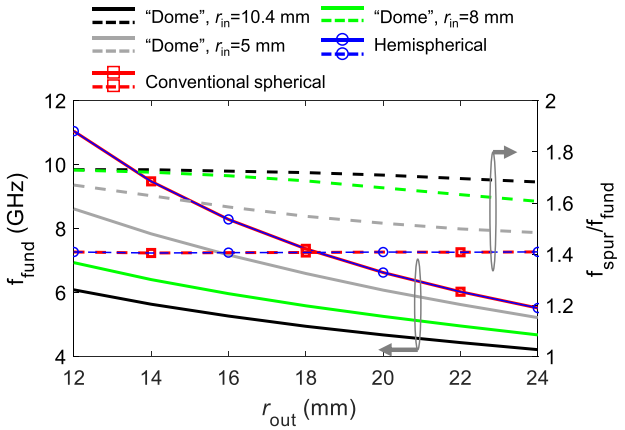

FIGURE 2. **Resonant frequency of the fundamental mode f_{fund} and the ratio of the first spurious mode to the fundamental mode f_{spur}/f_{fund} for the proposed dome-shaped resonator, the conventional spherical resonator, and the hemispherical resonator for alternative outer radius rout with different r_{in}.**

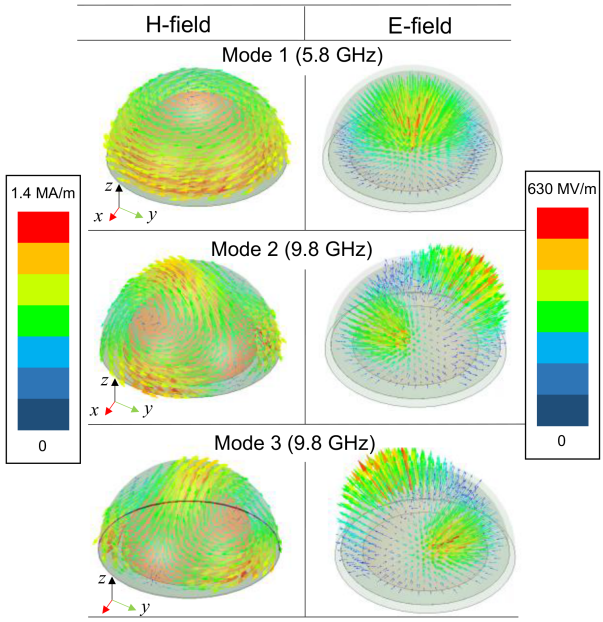

FIGURE 3. **Magnetic and electric field distribution of the first three resonant modes of the proposed dome-shaped resonator obtained with eigenmode simulations in ANSYS HFSS. From top to bottom: Mode 1, Mode 2, Mode 3.**

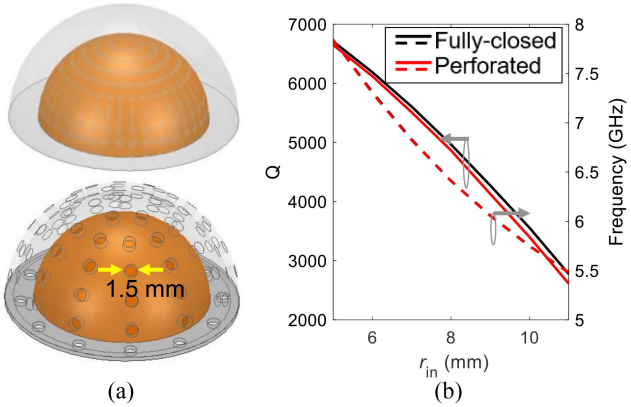

FIGURE 4. **(a) 3D geometries of a fully-enclosed and a perforated dome-shaped resonator to facilitate Cu platting. (b) *Q* and frequency of the fundamental mode for different rin showing minimal radiation loss caused by the holes (r_{out} = 14 mm). Cu is considered as metallization material.**

conventional spherical and the hemispherical resonator are also shown in this figure for comparison purposes alongside their simulated *Q* which have been obtained through eigen-mode simulations in ANSYS HFSS. The denoted *Q* values were obtained with eigenmode simulations considering bulk copper without any surface roughness. Specifically, the capacitively-loaded dome-shaped resonator is created by loading a hollow hemispherical resonator with outer radius r_{out} with a concentric fully metallic hemisphere with a radius r_{in} as shown in Fig. 1(c). Due to the capacitive loading, the resonant frequency of the fundamental mode will be lower than the one of the spherical and the hemispherical resonator as shown in Fig. 2. Thus, if designed for the same resonant frequency (e.g., 5.8 GHz), the dome-shaped resonator will be having a smaller volume than the spherical resonator as shown in Fig. 1. Specifically, for a $r_{out}/r_{in} = 1.35$, an 85% smaller volume is occupied whilst exhibiting a 54% higher *Q*/Vol than the conventional spherical resonator demonstrating the advantages of the proposed dome-shaped configuration. This ratio is chosen for all the BPF designs in this manuscript as a compromise between high *Q*, small size and wide spurious-free response.

The magnetic field distribution of the first three modes of the dome-shaped resonator is illustrated in Fig. 3. As shown in Fig. 3(a), the fundamental mode (mode 1) in the dome resonator is a quasi-TM_{101} mode. The first higher order modes are a pair of degenerate modes, i.e., a quasi-TM_{201A} and quasi-TM_{201B} [31] that have a different polarization direction. Figure 2(a) shows the frequency of the fundamental mode f_{fund} and its ratio to the first higher order degenerate modes (mode 2, 3) $f_{2,3}/f_{fund}$ of the capacitively-loaded dome resonator, the conventional spherical and the hemispherical resonator for different outer radius r_{out}. As it can be seen, the fundamental modes of the conventional spherical and hemispherical resonators are located at the same frequency which is significantly higher than the one of the dome-shaped resonators for the same size, indicating the miniaturization advantages of the proposed resonator concept. Furthermore, the $f_{2,3}/f_{fund}$ ratio for the proposed dome resonator is about 1.7:1, which is larger than that of the conventional spherical or hemispherical resonator denoting that when utilized in BPFs, their out-of-band response will have a wider spurious-free range as an advantage to be highlighted.

To facilitate monolithic integration for the proposed dome-shaped resonator concept, its outer walls need to be perforated to allow for the inner walls and internal structures to be metalized. Therefore, multiple holes with diameter of 1.5 mm are added to the outer cavity wall as shown in Fig. 4(a). As noted in Fig. 4(b), the resonator's *Q* remains unchanged before and

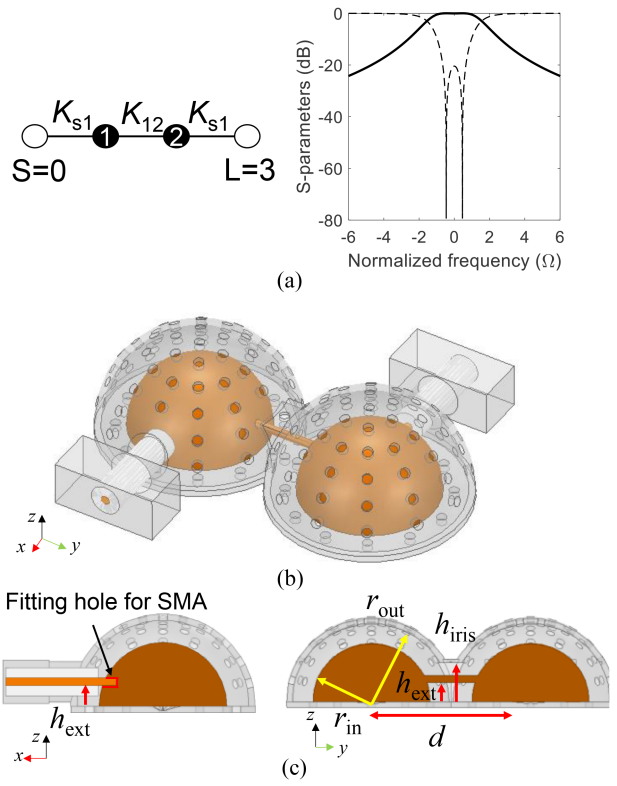

FIGURE 5. (a) Coupling routing diagram and synthesized response of the second-order BPF with horizontally coupled dome-shaped resonators. $m_{s1} = 1.1$, $m_{12} = 1$. (b) Bird-eye view of the second-order BPF. (b) Side views. $r_{in} = 10.4$, $r_{out} = 14$, $h_{ext} = 4$, $h_{iris} = 7$, $d = 28$, all units are in mm.

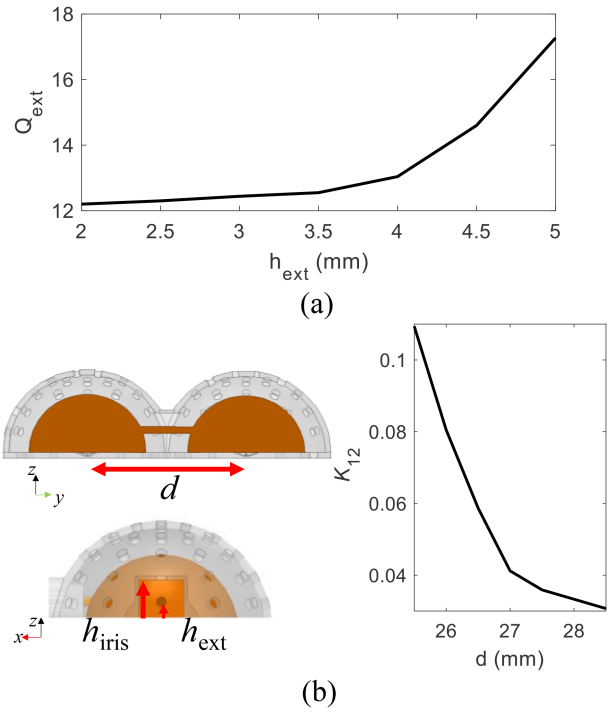

FIGURE 6. (a) External coupling Q_{ext} as a function of h_{ext}. (b) Inter-resonator coupling detail and extracted K_{12} for alternative distances d.

after adding the holes for small r_{in}. A minor Q degradation is only observed for larger r_{in} due to the high E-field concentration between the two concentric hemi-spheres.

B. SECOND-ORDER BPF DESIGN

To validate the proposed dome resonator concept, a second-order BPF geometry is considered. The coupling routing diagram (CRD), theoretically synthesized response and the 3D model of the BPF are shown in Fig. 5(a) and (b). It should be noted that higher order modes including Mode 2, 3 are omitted in the CRD as they do not contribute to the passband response. As it can be seen, the filter is designed by coupling two dome-shaped resonators in the same horizontal plane. In particular, the external coupling (Q_{ext}) is materialized by tapping the inner connector of the SMA to the inner hemisphere of the dome as shown in Fig. 5(c), where its strength is controlled by the height of the tapping location h_{ext}. Using full-wave EM simulations, Q_{ext} can be extracted for different values of h_{ext} as shown in Fig. 6(a). In particular, a higher h_{ext} will result in larger Q_{ext}. The inter-resonator coupling (K_{12}) is realized by connecting the inner hemispheres of adjacent dome resonators by a short metallic rod within a coupling iris as detailed in Fig. 5(c). The details of the coupling iris and the extracted K_{12} are provided in Fig. 6(b). As shown, the value of K_{12} is mainly affected by the distance of the two resonators d, and a larger d will result in smaller coupling as illustrated in Fig. 6(b).

It is worth noticing that the location of the RF excitation (i.e., the SMA connector) may affect the coupling to the higher order modes i.e., Mode 2 and 3 that may appear as spurious modes as illustrated in Fig. 7(a) for the case of a BPF that was designed for a center frequency $f_c = 5.8$ GHz and fractional bandwidth (FBW) = 5.5%. Specifically, in the in-line SMA port configuration (Fig. 7(a), left), Mode 2 will be excited in each resonator due to the H-field of the RF excitation aligning with the field maximum of the mode. Furthermore, the two Mode 2 resonances will be coupled through the coupling iris, generating spurious band as shown in Fig. 7(b). On the contrary, Mode 3 will not be excited since the SMA is pointing at the field null. For the case of the offset SMA port configuration (Fig. 7(a), right), Mode 2 will not be excited due to the RF excitation being located at the minimum of the H-field. Mode 3 can be excited in each resonator, however due to the inter-resonator coupling between the two resonators being weak (the coupling iris is located at the field minimal), transmission is minimized at these frequencies. A similar technique has been discussed in [22] for spherical resonators-based BPFs. Using this configuration, the out-of-band suppression bandwidth of the BPF can be enlarged by suppressing the higher order modes as demonstrated in the EM simulated S-parameter performance in Fig. 7(b). As it can be seen, a spurious resonance is observed at 9.4 GHz, which is 1.65 times larger than the passband frequency.

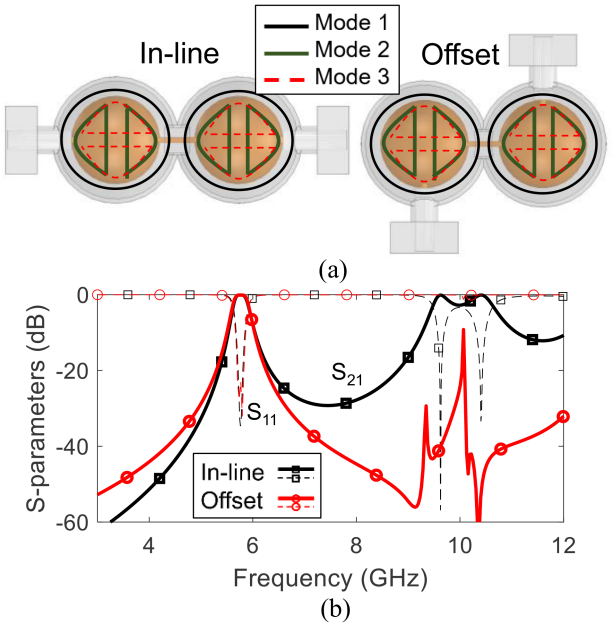

FIGURE 7. (a) Magnetic field distribution of the modes in both in-line and offset-port configuration. (b) Wideband EM simulated S-parameters of the second-order BPF for two different RF port orientations (in-line and offset) with the offset one facilitating spurious suppression.

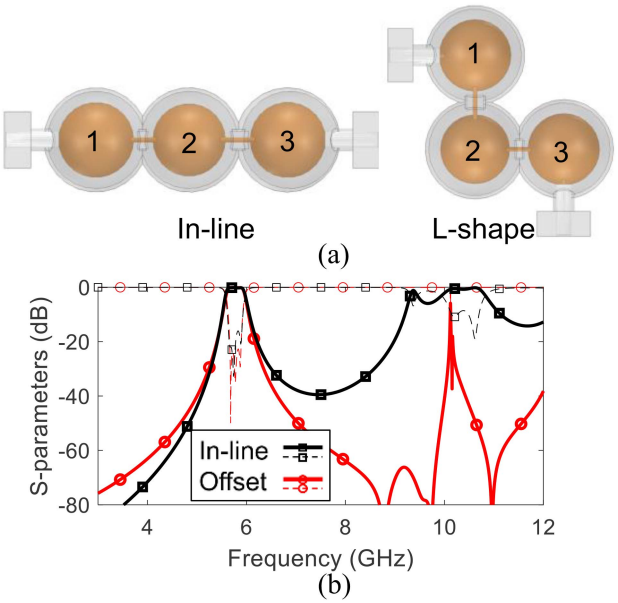

FIGURE 9. (a) In-line and L-shape resonator arrangement for the third-order BPF. (b) Wideband S-parameter response of third-order BPF for different resonator arrangements (in-line and L-shape) with the L-shaped arrangement leading to a wider out-of-band suppression.

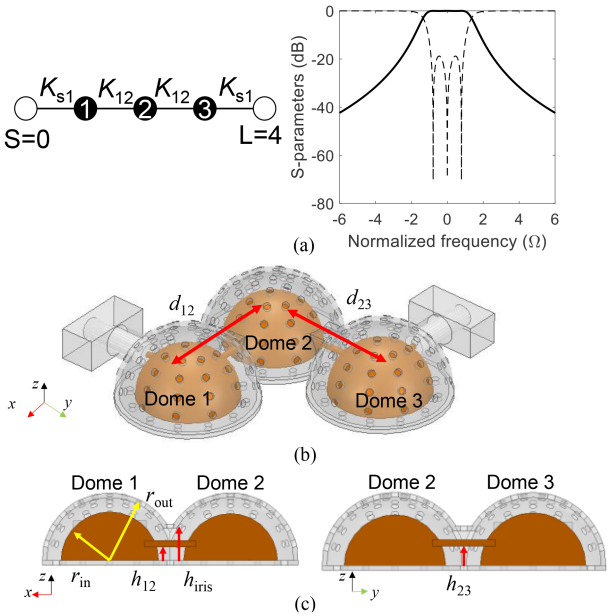

FIGURE 8. (a) Coupling routing diagram and synthesized response of the third-order BPF. (b) Bird-eye view of the third-order BPF using dome-shaped resonators (c) Side views. r_{in} = 10.4, r_{out} = 14, h_{ext} = 4, h_{12} = 4.6, h_{23} = 3.7, h_{iris} = 7, d_{12} = 26.4, d_{23} = 28, all units are in mm.

C. THIRD ORDER BPF DESIGN

To further explore the scalability of the proposed BPF configuration to higher-order transfer functions, a third-order BPF with f_c = 5.8 GHz and FBW = 6.5% was designed using similar design guidelines as above. The CRD, synthesized response, and 3D model of the third-order BPF is demonstrated in Fig. 8. Likewise in this case, alternative resonator arrangements can be selected to realize the third-order transfer function. For example, the three resonators can be placed in an in-line or an L-shape configuration where resonator 1, 2 is orthogonal to resonator 2, 3 as shown in Fig. 9. Although both configurations can be chosen, the L-shape arrangement exhibits higher upper stopband rejection due to the inter-resonator coupling for the Mode 2 and 3 resonances being minimized for the same reason as in the second-order BPF case outlined in Section II-B. In this case and as shown in Fig. 9(b), two transmission zeros (TZs) are observed at 8.78 GHz and 9.8 GHz for the L-shaped configuration. As a result, the 20-dB upper stopband is extended to 10.10 GHz, which is 1.02 GHz higher than the in-line configuration (that extends up to 8.98 GHz) and 1.75 times higher than the passband center frequency. Furthermore, the stopband rejection of the L-shaped BPF is significantly higher than the one of the in-line configuration at the higher side of the passband, whereas the rejection ratio remains similar at the lower side. Therefore, the L-shaped configuration is selected for realizing the third-order BPF.

D. SECOND-ORDER VERTICALLY-STACKED "BALL"-SHAPED BPF

For compact integration purposes, a vertically-stacked "ball-shaped" configuration is investigated for the realization of the second-order BPF. In this case, two resonators are attached back-to-back using a shared ground plane as shown in Fig. 10. A small slot with angle ϕ is opened in the shared ground plane to facilitate mixed EM-coupling between the two of the fundamental modes. Furthermore this "ball"-shaped configuration results in a new higher order and higher frequency mode,

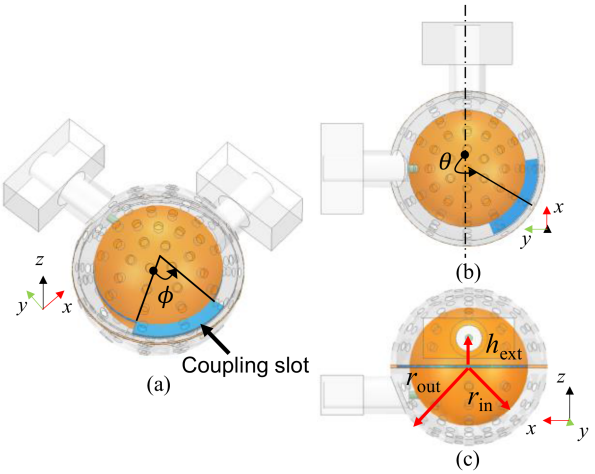

FIGURE 10. (a) Bird-eye view of the vertically-stacked second-order "ball"-shaped BPF using two vertically-stacked dome-shaped resonators. (b) Top view. (c) Side view. The blue area indicates the coupling slot. The design parameters are: $r_{in} = 10.4$ mm, $r_{out} = 12.8$ mm, $\theta = 40°$, $\phi = 80°$, $h_{ext} = 4.75$ mm.

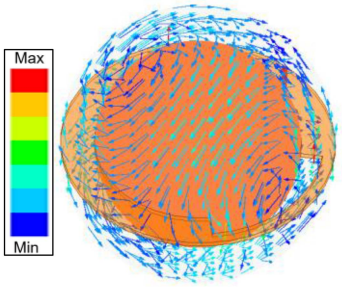

FIGURE 11. H-field distribution at 9 GHz showing an additional mode (mode 4) resonating within the entire volume of the ball-shaped filter. It is excited due to the presence of the slot as a result of the vertical stacking and the coupling iris.

namely Mode 4, that resonates within the volume of the entire filter and is provided in Fig. 11. This mode should be distinguished from Mode 2 and 3 in Fig. 3, as it is unique to the "ball"-shaped structure of the BPF. Therefore, an alternative CRD can be proposed for the "ball"-shaped BPF as shown in Fig. 12(a) with its synthesized S-parameters provided in Fig. 12(b). In this case, Mode 4 is included in the CRD to model its effect to the TZs near the passband, while other higher modes including Mode 2 and 3 are omitted. As it can be seen, two TZs, namely TZ_1 and TZ_2, appear in the higher side of the passband, where TZ_1 is generated by the mixed EM coupling and TZ_2 is due to the existence of Mode 4 in Fig. 11 which is modelled by node 3 in the CRD.

The EM-simulated response of the vertically-stacked BPF (designed for $f_c = 5.9$ GHz and FBW $= 10\%$) is depicted in Fig. 13 and shows a good agreement with the theoretically synthesized response in Fig. 12(b), validating the feasibility of the proposed CRD. The inter-resonator coupling at the passband K_{12} is extracted using EM simulations for different slot angles ϕ and is provided in Fig. 14(a) with larger slots resulting in higher K_{12}. Furthermore, Fig. 14(b) demonstrates

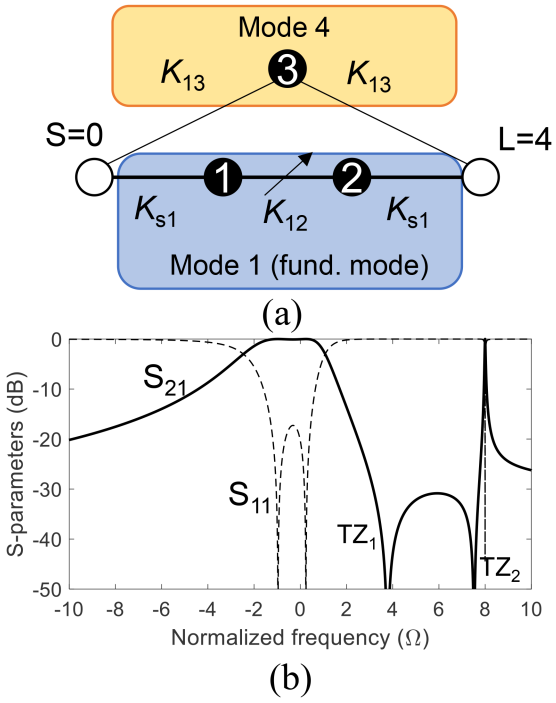

FIGURE 12. (a) CRD of the "ball"-shaped BPF. Node 1, 2 represent the fundamental mode and node 3 represents the additional mode in Fig. 11. (b) Synthesized S-parameter showing two TZs and a spurious band due to mode 4.

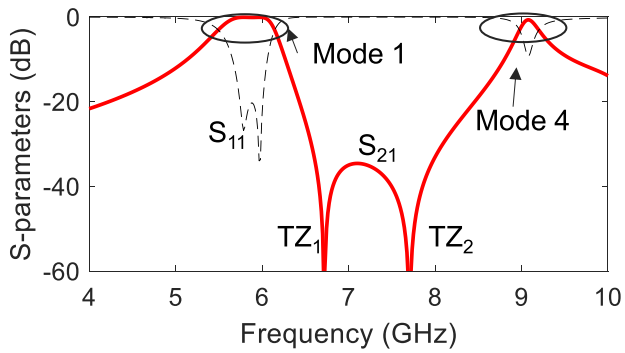

FIGURE 13. EM-simulated response of the vertically-stacked second-order ball-shaped BPF.

the frequencies of the TZs as a function of the location of the slot denoted by the relative angle θ between the SMA center and the middle of the slot as illustrated in Fig. 10(b). It can be observed that when the slot is placed in between the two SMA ports, i.e., $0° < \theta < 90°$, both TZs can be placed above and close the passband. Specifically, when $\theta = 0°$ or $90°$, TZ_1 is closest to the passband; however, when $\theta = 45°$, TZ_2 will be closest to the passband but always above it. As the slot moves away from the SMA port, i.e., $\theta > 90°$, both TZs will move to higher frequencies away from the passband. Therefore, the TZs can be designed at the desired frequencies using the guidelines in Fig. 14(b). In this work, $\theta = 40°$ is chosen such that both TZs can be present close and above the passband, which creates a

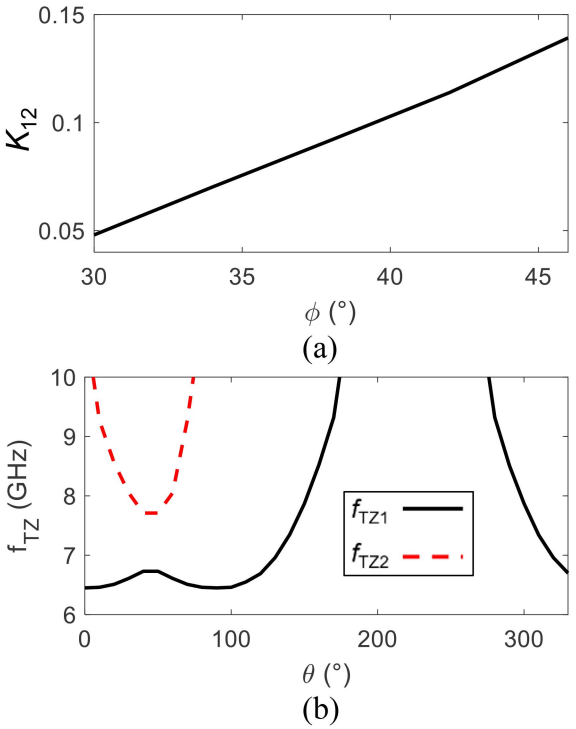

FIGURE 14. (a) K_{12} as a function of ϕ. (b) TZ frequencies as a function of θ.

two-pole/two-TZ response, increasing the out-of-band rejection of the BPF. Using the aforementioned design guidelines, a two-pole/two-TZ ball-shaped BPF was designed with the following specifications: center frequency $f_c = 5.9$ GHz, FBW $= 10\%$, location of the TZs: $f_{TZ1} = 6.7$ GHz, $f_{TZ2} = 7.7$ GHz.

III. EXPERIMENTAL VALIDATION

To validate the miniaturized dome resonator-based BPF concept, three filter prototypes: i) a second order BPF with offset feeding, $f_c = 5.8$ GHz and FBW $= 5.5\%$, ii) a third order L-shaped BPF with $f_c = 5.8$ GHz and FBW $= 6.5\%$, and iii) a second-order "ball"-shaped BPF with $f_c = 5.9$ GHz and FBW $= 10\%$ were designed, manufactured, and tested. Monolithic SLA-based integration was considered for all of the three filters and a commercially available 50 μm thick ($>20\times$ skin depth at operating frequency) Cu-plating process was employed for metallization. To be able to manufacture the filters monolithically, their geometries need to be properly oriented in the SLA built platform of a commercially-available desktop size printer to avoid generating any internal support structures. The CAD model of the second-order BPF for SLA printing is depicted in Fig. 15(a). As shown, all the support structures are generated beneath the filter volume and can be easily removed after the printing process. The manufactured second-order dome resonator-based BPF before and after Cu-plating is shown in Fig. 15(b). Its RF measured response was characterized with a Keysight N5224A PNA and is shown in Fig. 16. It is summarized as follows: center frequency $f_c = 5.76$ GHz, minimal in-band IL $= 0.37$ dB, FBW $= 5.45\%$, corresponding to an effective quality factor (Q_{eff}) $= 890$.

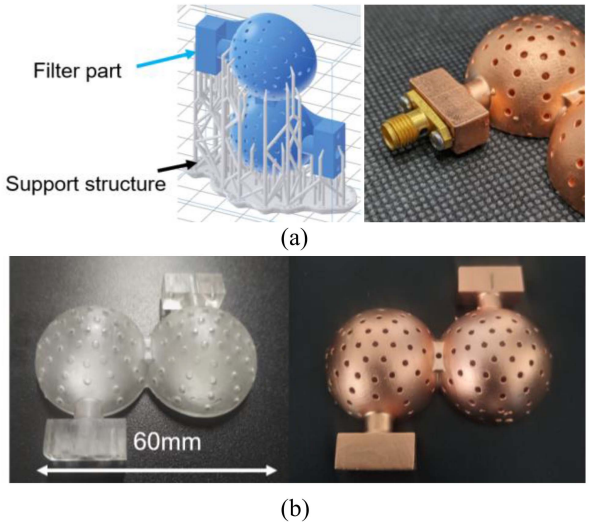

FIGURE 15. (a) CAD model for SLA 3D printing of the second-order BPF and detail of the SMA connector assembly. (b) Manufactured prototype before and after Cu-plating.

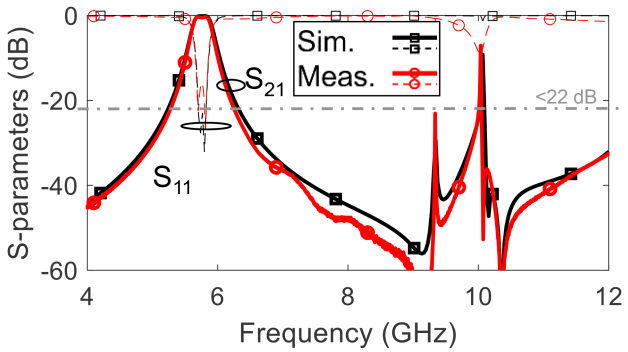

FIGURE 16. RF-measured and EM-simulated response of the second-order capacitively-loaded dome resonator-based BPF shown in Fig. 15.

The 20 dB upper-stopband was measured up to 10.14 GHz ($1.76f_c$). As shown, a decent agreement has been achieved between the EM simulations and the RF measurements successfully validating the proposed dome-shaped BPF concept.

The CAD model for SLA printing, and the manufactured prototype of the third-order BPF before and after Cu-plating are demonstrated in Fig. 17(a) and (b). Its corresponding simulated and measured S-parameters are depicted in Fig. 18. The RF measured transfer function exhibits: $f_c = 5.80$ GHz, minimal in-band IL $= 0.28$ dB, FBW $= 6.48\%$, corresponding to $Q_{eff} = 1230$, and its 20 dB upper-stopband was measured up to 10.10 GHz ($1.74f_c$). As shown, a good agreement can be observed between the EM-simulated ($f_c = 5.80$ and FBW $= 6.5\%$, in-band IL $= 0.14$ dB, $Q_{eff} = 2200$, 20 dB upper-stopband: $1.74f_c$) and the RF-measured performance, successfully validating the proposed miniaturized dome resonator-based BPF concept. The observed Q_{eff} reduction in the RF measurements in relation to the one predicted in eigenmode simulations is attributed to imperfections in the SMA connector assembly and the surface roughness of

TABLE 1. Comparison With State-of-the-art Spherical and Capacitively-Loaded Cavity BPFs

Ref.	Res. Type	Order	Tech	Mono.	f_c (GHz)	FBW (%)	f_{spur}/f_c	Res. Size (λ_0^3)	Q_{eff}	Q/Vol
[7]	Sphere	4	SLA	Yes	10	3	1.27	0.289	3800	13150
[8]	Sphere	2	SLA	Yes	12/12.5	1/1.9	1.28	0.268	2400	8950
[9]	Sphere	2	SLM	Yes	11.5	0.47	N/A	0.349	2900	8310
[13]	Sphere	3	CNC	No	6.5	1.9	1.28	N/A	8000	N/A
[16]	Hemisphere	2	PolyJet	No	4.8-5.2	3.3/5.2	N/A	0.114	100-650	880-5700
[17]	Slotted sphere	4	DMLS	Yes	10.1	3	1.8	0.164	780-1450	4760-88840
[18]	Hemisphere	4	SLA	Yes	32	3	1.38	0.161	2000	12420
[30]	Coaxial	2	SLA	Yes	3.7	8.1	N/A	0.016	1000	62500
[32]	Conical	4	SLA	No	1.7	10	3.58	0.006	100	15630
[33]	Ridged-WG	4	CNC	No	10.1	2	1.37	0.21	4800	22850
[34]	"Mushroom"	4	SLA	No	0.8	10	N/A	N/A	N/A	N/A
TW	Dome	2	SLA	Yes	5.8	5.5	1.73	0.041	890	21700
TW	Dome	3	SLA	Yes	5.8	6.5	1.74	0.041	1230	30000
TW	Dome	2	SLA	Yes	5.9	10	1.50	0.041	720	17560

(Mono.: Monolithically-integrated; Res. Size: size of a single resonator; f_{spur}: first spurious resonance with magnitude >-20 dB)

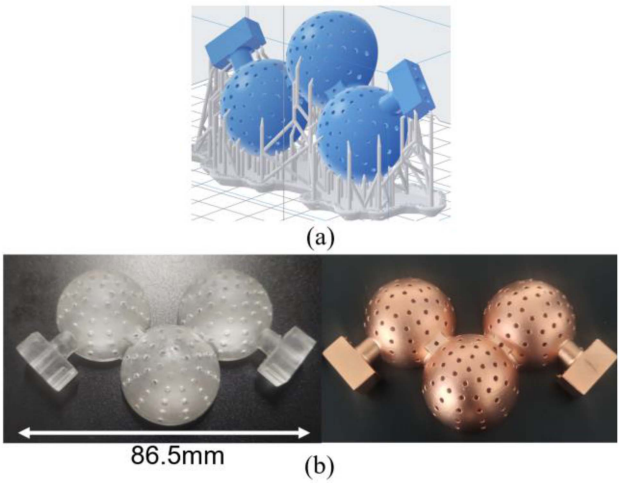

FIGURE 17. (a) CAD model of the third-order BPF for SLA printing. (b) Manufactured prototype before and after Cu-plating.

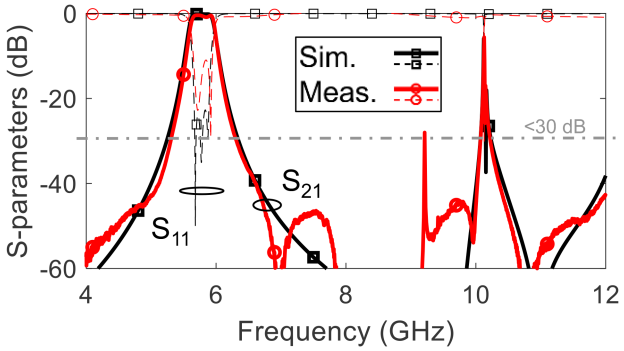

FIGURE 18. RF-measured and EM-simulated response of the third-order dome resonator-based BPF shown in Fig. 17.

the metalized walls that haven't been considered in the ideal simulation model.

Fig. 19 exhibits the CAD model and the manufactured prototype of the second-order vertically-stacked "ball"-shaped BPF. The measured S-parameters are shown in Fig. 20 alongside the EM simulated ones and appear to be in good agreement. Specifically, the RF measured transfer function exhibits: $f_c = 5.90$ GHz, minimal in-band IL = 0.22 dB, FBW = 10.0%, corresponding to $Q_{eff} = 720$. The location of the TZs were measured at $f_{TZ1} = 6.74$ GHz, $f_{TZ2} = 7.81$ GHz.

To evaluate the effectiveness of the proposed dome-shaped BPF concept in relation to state-of-the-art spherical and hemispherical resonator-based BPFs, a comparison is provided in in Table 1. As it can be seen, the proposed filter concept is uniquely presented in this manuscript for the first time and is the only one using miniaturized "dome" resonators. Specifically, the volume of the dome resonator is 84–88% smaller than that of the spherical resonator in [7], [8], [9], and 64-74% smaller than the hemispherical resonator shown in [16], [17], [18]. In addition, the spurious-free range ($1.74f_c$) of the proposed dome-resonator-based filters is significantly higher than that of the spherical or hemispherical filters, e.g., [7],

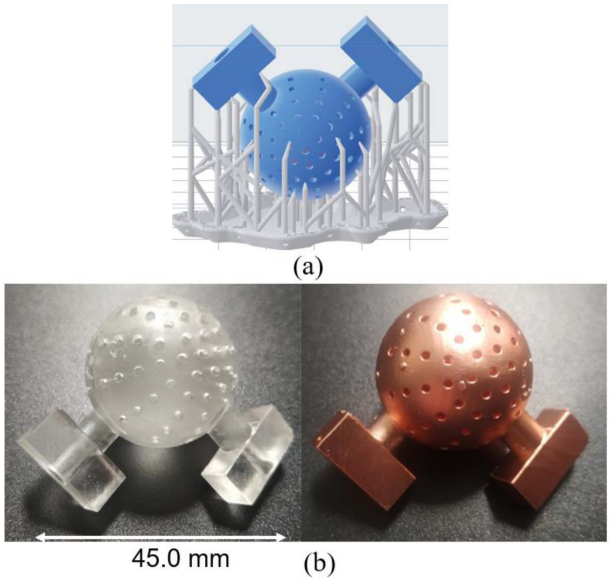

FIGURE 19. (a) CAD model of the second-order "ball"-shaped BPF for SLA printing. (b) Manufactured prototype before and after Cu-plating.

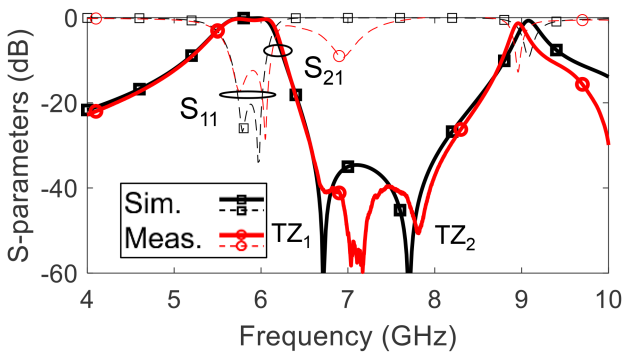

FIGURE 20. RF-measured and EM-simulated response of the second-order dome resonator-based BPF shown in Fig. 19.

[8], [13], [18], which is typically around $1.3f_c$. Although the Q_{eff} of the dome resonator is lower compared to the spherical resonator, its Q_{eff}/Vol is higher (17560–30000 in the measured result), and a relatively high Q_{eff} of 720–1230 is obtained. In relation to other 3D BPF topologies, Table 1 also provides a comparison with coaxial, conical and ridge-waveguide BPFs. As evidenced, coaxial or conical cavity resonator-based BPFs may lead to smaller volume due to stronger capacitive loading as in [30] and [32], however they are based on small capacitive gaps (100 s of μm) that limit the power handling capacity due to the same reason. Furthermore, whereas the coaxial-resonator based BPFs have comparable Q_{eff}, the conical BPFs exhibit 7-12x smaller Q_{eff}s. Compared to other capacitively-loaded BPFs, e.g., the ridge waveguide in [33], the dome-shaped BPF in this work exhibits smaller size and better spurious performance.

IV. CONCLUSION

This paper presented a new class of highly-miniaturized dome-shaped resonator-based BPFs. Size reduction is achieved by using: i) a capacitively-loaded hemispherical cavity dome-shaped resonators, ii) monolithic SLA 3D printing-enabled integration, and iii) vertical resonator stacking. The proposed dome resonator concept leads to 85% smaller resonators compared to conventional spherical configurations and can be exploited for the realization of low IL BPFs with wide spur suppression. For proof-of-concept validation purposes, a second-, a third-order, and a second-order vertically-stacked BPF prototypes operating at 5.8 GHz and 5.9 GHz were designed, manufactured and tested. Furthermore, an L-shaped BPF configuration has been proposed to further improve the spurious suppression and stopband rejection.

REFERENCES

[1] R. R. Mansour, "Filter technologies for wireless base stations," *IEEE Microw. Mag.*, vol. 5, no. 1, pp. 68–74, Mar. 2004.
[2] T. R. Jones and M. Daneshmand, "Miniaturized slotted bandpass filter design using a ridged half-mode substrate integrated waveguide," *IEEE Microw. Wireless Compon. Lett.*, vol. 26, no. 5, pp. 334–336, May 2016.
[3] M. S. Bakr, I. C. Hunter, and W. Bösch, "Miniature Triple-Mode Dielectric Resonator Filters," *IEEE Trans. Microw. Theory Techn.*, vol. 66, no. 12, pp. 5625–5631, Dec. 2018.
[4] K. Wakino, T. Nishikawa, and Y. Ishikawa, "Miniaturization technologies of dielectric resonator filters for mobile communications," *IEEE Trans. Microw. Theory Techn.*, vol. 42, no. 7, pp. 1295–1300, Jul. 1994.
[5] G. Goussetis and D. Budimir, "Compact ridged waveguide filters with improved stopband performance," in *Proc. IEEE MTT-S Int. Microw. Symp.*, 2003, pp. 953–956.
[6] E. B. Lima, J. R. Costa, and C. A. Fernandes, "Wideband and high-selectivity dual-band filter for Ka-band satellite antennas," *IEEE Antennas Wireless Propag. Lett.*, vol. 16, pp. 1627–1630, Jan. 2017.
[7] C. Guo, X. Shang, J. Li, F. Zhang, M. J. Lancaster, and J. Xu, "A lightweight 3-D printed X-band bandpass filter based on spherical dual-mode resonators," *IEEE Microw. Wireless Compon. Lett.*, vol. 26, no. 8, pp. 568–570, Aug. 2016.
[8] Y. Chen et al., "3-D printed dual-band filter based on spherical dual-mode cavity," *IEEE Microw. Wireless Compon. Lett*, vol. 31, no. 9, pp. 1047–1050, Sep. 2021.
[9] L. Qian et al., "A narrowband 3-D printed invar spherical dual-mode filter with high thermal stability for OMUXs," *IEEE Trans. Microw. Theory Techn.*, vol. 70, no. 4, pp. 2165–2173, Apr. 2022.
[10] X. Wen et al., "An invar alloy SLM printed diplexer with high thermal stability," *IEEE Trans. Circuits Syst. II, Exp. Briefs*, vol. 69, no. 3, pp. 1019–1023, Mar. 2022.
[11] X. Wen et al., "SLM printed waveguide dual-mode filters with reduced sensitivity to fabrication imperfections," *IEEE Microw. Wireless Compon. Lett.*, vol. 31, no. 11, pp. 1195–1198, Nov. 2021.
[12] D. R. Hendry and A. M. Abbosh, "Parallel multimode cavity filters with generalized frequency response," *IEEE Trans. Microw. Theory Techn.*, vol. 67, no. 5, pp. 1844–1853, May 2019.
[13] B. Gowrish, S. K. Koul, and R. R. Mansour, "Transversal coupled triple-mode spherical resonator-based bandpass filters," *IEEE Microw. Wireless Compon. Lett.*, vol. 31, no. 4, pp. 369–372, Apr. 2021.
[14] L. Sheng-Li and L. Wei-Gan, "A five mode single spherical cavity microwave filter," in *Proc. IEEE MTT-S Microw. Symp.*, Jun. 1992, pp. 909–912.
[15] J. Li, Z. Chen, and T. Yuan, "Optimized design of a miniaturized irregular spherical resonator with enhanced subtractive/additive manufacturing process compatibility," in *Proc. IEEE MTT-S Int. Wireless Symp.*, Sep. 2020, pp. 1–3.
[16] A. Olaru, N. Delmonte, S. Marconi, G. Alaimo, F. Auricchio, and M. Bozzi, "Tunable microwave filter based on hemispherical 3D-printed resonators," in *Proc. IEEE 24th Int. Microw. Radar Conf.*, Sep. 2022, pp. 1–4.

[17] J. Li, K.-D. Hong, and T. Yuan, "Slotted hemispherical resonators for 3-D printed waveguide filters with extended spurious-free stopbands," *IEEE Access*, vol. 7, pp. 130221–130235, Sep. 2019.
[18] J. Li, C. Guo, L. Mao, J. Xiang, G.-L. Huang, and T. Yuan, "Monolithically 3-D printed hemispherical resonator waveguide filters with improved out-of-band rejections," *IEEE Access*, vol. 6, pp. 57030–57048, Sep. 2018.
[19] R. V. Snyder, G. Macchiarella, S. Bastioli, and C. Tomassoni, "Emerging trends in techniques and technology as applied to filter design," *IEEE J. Microwaves*, vol. 1, no. 1, pp. 317–344, Jan. 2021.
[20] D. Miek, S. Simmich, F. Kamrath, and M. Höft, "Additive manufacturing of E-plane cut dual-mode X-band waveguide filters with mixed topologies," *IEEE Trans. Microw. Theory Techn.*, vol. 68, no. 6, pp. 2097–2107, Jun. 2020.
[21] M. D'Auria et al., "3-D printed metal-pipe rectangular waveguides," *IEEE Trans. Compon. Packag. Manuf. Technol.*, vol. 5, no. 9, pp. 1339–1349, Sep. 2015.
[22] C. Guo, X. Shang, M. J. Lancaster, and J. Xu, "A 3-D printed lightweight X-band waveguide filter based on spherical resonators," *IEEE Microw. Wireless Compon. Lett.*, vol. 25, no. 7, pp. 442–444, Jul. 2015.
[23] T.-H. Chio, G.-L. Huang, and S.-G. Zhou, "Application of direct metal laser sintering to waveguide-based passive microwave components, antennas, and antenna arrays," *IEEE Proc.*, vol. 105, no. 4, pp. 632–644, Apr. 2017.
[24] O. A. Peverini et al., "Selective laser melting manufacturing of microwave waveguide devices," *Proc. IEEE*, vol. 105, no. 4, pp. 620–631, Apr. 2017.
[25] C. Guo et al., "Shaping and slotting high-Q spherical resonators for suppression of higher order modes," in *Proc. IEEE MTT-S Int. Microw. Symp.*, Jun. 2019, pp. 1205–1208.
[26] F. Zhang et al., "A 3-D printed bandpass filter using $TM_{2\,1\,1}$-mode slotted spherical resonators with enhanced spurious suppression," *IEEE Access*, vol. 8, pp. 213215–213223, Nov. 2020.
[27] F. Zhang et al., "3-D printed slotted spherical resonator bandpass filters with spurious suppression," *IEEE Access*, vol. 7, pp. 128026–128034, Sep. 2019.
[28] F. Calignano, D. Manfredi, E. P. Ambrosio, L. Iuliano, and P. Fino, "Influence of process parameters on surface roughness of aluminum parts produced by DMLS," *Int. J. Adv. Manuf. Technol.*, vol. 67, no. 9, pp. 2743–2751, Aug. 2013.
[29] F. L. Borgne, G. Cochet, J. Haumant, D. Diedhiou, K. Donnart, and A. Manchec, "An integrated monobloc 3D printed front-end in Ku-band," in *Proc. IEEE 49th Eur. Microw. Conf.*, Oct. 2019, pp. 786–789.
[30] K. Zhao and D. Psychogiou, "Monolithic multiband coaxial resonator-based bandpass filter using stereolithography apparatus (SLA) manufacturing," *IEEE Trans. Microw. Theory Techn.*, vol. 70, no. 9, pp. 4156–4166, Sep. 2022.
[31] K. Zhang and D. Li, *Electromagnetic Theory for Microwaves and Optoelectronics*, 2nd ed. Berlin, Germany: Springer, 2008.
[32] E. Lopez-Oliver et al., "3-D-Printed compact bandpass filters based on conical posts," *IEEE Trans. Microw. Theory Techn.*, vol. 69, no. 1, pp. 616–628, Jan. 2021.
[33] S. Bastioli, L. Marcaccioli, and R. Sorrentino, "Compact dual-mode rectangular waveguide filters using square ridge resonators," *Int. J. Microw. Wireless Techn.*, vol. 1, no. 4, pp. 241–247, 2009.
[34] C. Tomassoni et al., "Compact quasi-elliptic filters with mushroom-shaped resonators manufactured with 3-D printer," *IEEE Trans. Microw. Theory Techn.*, vol. 66, no. 8, pp. 3579–3588, Aug. 2018.